IEEE Access
Multidisciplinary | Rapid Review | Open Access Journal

Received 20 June 2023, accepted 19 July 2023, date of publication 24 July 2023, date of current version 1 August 2023.

Digital Object Identifier 10.1109/ACCESS.2023.3298221

RESEARCH ARTICLE

Design and Measurement of a Minuscule-Sized Implantable Antenna for Brain–Machine Interfaces

NAEEM ABBAS[1], SANA ULLAH[1], (Graduate Student Member, IEEE), ZUBAIR BASHIR[2], ABDUL BASIR[1], (Member, IEEE), AND HYOUNGSUK YOO[1], (Senior Member, IEEE)

[1]Department of Electronic Engineering, Hanyang University, Seoul 04763, South Korea
[2]Telecommunication Engineering Department, University of Engineering and Technology (UET), Taxila 47050, Pakistan

Corresponding author: Hyoungsuk Yoo (hsyoo@hanyang.ac.kr)

This work was supported by the Institute for Information and Communications Technology Promotion (IITP) Grant funded by the Korean Government, through the Ministry of Science, and Information and Communications Technology (ICT) and Future Planning (MSIP), under Grant 2022-0-00310.

ABSTRACT The study proposes a small dual-band implantable antenna for brain-machine interface (BMI) working over industrial, scientific, and medical (915 MHz, 2.45 GHz) bands. The antenna's flexibility and small size allow for easy integration into implantable devices, while its dual-band resonance enables power-efficient operation. Through parametric analysis and optimization, the antenna achieves miniaturization without compromising performance. Slitted ground and patch and shorting pins techniques are used to achieve dual-band operation with miniaturized sizes of the antenna and BMI device of 9.8 mm^3 and 420 mm^3, respectively. For a practical scenario, a seven-layer brain model with different layers and a realistic head model were used to analyze the performance of the antenna in heterogeneous environments. The calculated maximum specific absorption rate (SAR) values satisfied the IEEE safety standards C95.1-1999 and C95.1-2005 for implantable medical devices if the maximum radiated powers are under 10.1 and 8.1 mW at 915 and 2450 MHz, respectively. To verify the simulated results, the fabricated prototype underwent testing with minced pork meat, yielding impressive impedance bandwidths of 165 MHz and 625 MHz. The measurements revealed significant gains of -28.3 dBi and -18.5 dBi at frequencies of 915 MHz and 2.4 GHz, respectively. These findings validate the accuracy of the simulations without any deviations. Moreover, the link budget analysis results suggested that the antenna system can transmit a signal of up to 10 m at a data rate of 100 kbps.

INDEX TERMS Brain–machine interface (BMI), dual-band antenna, gain, implantable radios, impedance bandwidth, maximum allowable power, network analyzer, polyamide.

I. INTRODUCTION

The unprecedented technological evolution in implantable medical devices (IMDs) has attracted considerable interest in the development of devices that can reinforce the functionalities of paralyzed individuals. A recently developed technology known as the brain-machine interface (BMI) enables the recording and processing of neural data of a person and converts it into actions [1]. Using this technology, a disabled person can control prosthetic limbs and electronic appliances as well as perform small chores more independently in daily life [2], [3]. The BMI device comprises a sensor package, signal processor, software, battery, and power supply [25]. Additionally, an implantable antenna is embedded in the BMI to create a wireless link for continuous communication with an external component. This external unit includes a real-time device that maps the brain and effectively decodes neural activity into actions, as depicted in Fig. 1.

As a critical element within the BMI system, the implantable antenna is required to possess certain key characteristics in order to function effectively. These include a

The associate editor coordinating the review of this manuscript and approving it for publication was Dingguo Zhang.

This work is licensed under a Creative Commons Attribution-NonCommercial-NoDerivatives 4.0 License.
For more information, see https://creativecommons.org/licenses/by-nc-nd/4.0/

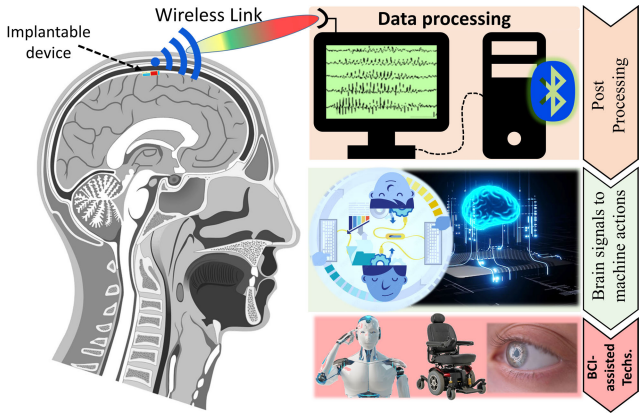

FIGURE 1. Wireless link overview, design and applications of implantable brain–machine-interface (BMI) devices.

minuscule size to facilitate accommodation within the device, a low specific absorption rate (SAR), a wide bandwidth, and adequate impedance matching [5], [6]. Consequently, the selection of an appropriate operational frequency for both the implanted antenna and the external receiver becomes paramount. Typically, medical devices and base stations establish connections through specific frequency bands, such as the MedRadio bands (403 MHz), as well as the industrial, scientific, and medical (ISM) bands (433 MHz, 915 MHz, and 2.45 GHz). However, the utilization of the MedRadio band is accompanied by limitations in terms of range and data rates due to its restricted operational bandwidth. Conversely, the ISM bands offer a broader range of applications, including wearable devices and various other technologies, and provide higher data rates. Therefore, for the purposes of this study, a dual-band operation at the ISM bands of 915 and 2400 MHz has been chosen. This selection allows for optimizing both data rates and range, facilitating enhanced performance and increased versatility in the context of BMI systems and related applications.

Multiple techniques have been conceived to develop high-performance minuscule implantable antennas. These include stacking radiation patches [7], employing high dielectric structures [8], and utilizing planar inverted-F antennas (PIFA). Additionally, slot etching on the ground plane and radiating patch has been explored to enhance the current path. For instance, a meandered-shape PIFA antenna was conceived for the 2.45 GHz ISM band, boasting a minuscule volume of 30.03 mm^3 [9]. In another study [10], a circular implantable antenna was suggested for the same frequency band and implanted in a seven-layer brain phantom. This antenna was designed on a low-permittivity substrate called Taconic RF-35, with a total volume of 39.3 mm^3. The simulated results revealed a bandwidth of 330 MHz and a peak gain of -20.75 dBi.

In the realm of medical devices, a circularly polarized spiral-shaped PIFA, operating at 610 MHz, was conceived in [11]. This antenna, designed on a 3.2 mm thick FR4 material,

TABLE 1. Comparison of the conceived antenna with state-of-the-art.

Ref.	Frequency (MHz)	Size (mm^3)	Bandwidth (MHz)	Gain (dBi)	SAR (W/kg) 1-g	Input Power (mW)	Device Study
[7]	402		27	-36.90	324.74	4.927	
	433	203.4	28	-35.99	309.74	5.166	No
	868		38	-35.14	296.94	5.388	
	915		40	-32.94	294.86	5.426	
[9]	2400	30.03	461	-28.65	682	2.3	No
[10]	2400	39.3	370	-20.75	568	2.8	No
[11]	610	251	10	-20	----	----	Yes
[12]	402		148	-30.5	588	2.72	
	1600	17.15	171	-22.6	441	3.62	Yes
	2450		219	-18.2	305	5.24	
[13]	433	23.6	168	-28.3	----	9.3	Yes
[14]	2450	9.8	1038.7	-20.71	289	4.56	No
[15]	2400	122	540	-33	486	7.2	No
[16]	400	797.96	153	-33.1	241.5	----	No
	2400		423	-14.5	149.5	----	
[18]	2450	7.8	480	-16.5	185.56	9.21	No
[25]	2450	50	80	-25	----	----	No
This	915		165	-28.3	158.4	10.10	
Work	2450	9.8	625	-18.5	197.2	8.11	Yes

had a total volume of 251 mm^3. Notably, it exhibited a realized peak gain of -20 dB and a bandwidth of 10 MHz. These advancements demonstrate the diverse strategies employed to achieve minuscule and high-performing implantable antennas for medical applications, particularly within the ISM frequency bands. Ongoing research and innovation in this field hold substantial potential for further enhancing the functionality and efficacy of implantable antennas in the context of biomedical devices.

A multiband spiral-shaped antenna was conceived for brain implantation in the MedRadio, Midfield, and 2.45 GHz ISM bands [12]. The antenna has a minuscule size of 17 mm^3; however, the narrow MedRadio bands make it difficult to reach the desired data rate. In [13], a circular multi-input multi-output (MIMO) antenna working in the 433 MHz band was conceived for implantable applications. The MIMO technology has since been utilized to increase the data rate of implantable antennas. Moreover, [14] conceived an ultra-wideband antenna operating at 2.45 GHz for scalp-based applications. This antenna used 0.1 a thick Rogers ULTRALAM dielectric material as the substrate and superstrate, respectively. This antenna had a volume of 9.8 mm^3 with 1038 MHz bandwidth and -20.7 a peak gain. However, these antennas have some limitations such as larger size, single band, and lower bandwidth. Therefore these antennas are not appropriate for the latest technologies for MBI.

To resolve the size and bandwidth issues, this study proposes a dual-band implantable antenna with two different ISM bands (902-928 MHz, 2.4-2.4835 GHz) for BMI applications. The dimensions of the conceived antenna were

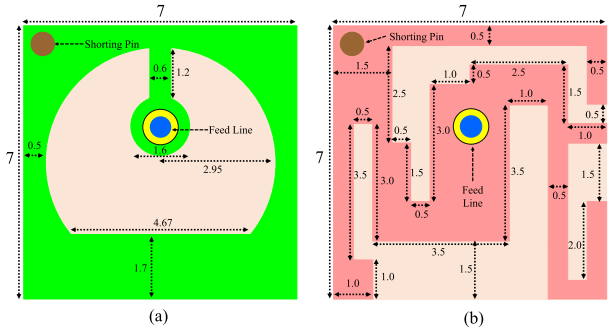

FIGURE 2. Footprints of the conceived dual-band antenna (unit: mm). (a) Radiating patch. (b) Ground plane.

7 mm × 7 mm × 0.2 mm and placed at 15 mm depth in a box of a homogeneous skin phantom (HSP) with a volume of 100 mm × 100 mm × 70 mm. For more precise and realistic results, the antenna performance was evaluated in a heterogeneous seven-layer brain model and a realistic head model. Final measurements of the fabricated prototypes were conducted using minced pork meat. A comparison of the conceived dual-band implantable antenna with the previously designed antennas is presented in Table 1. The conceived antenna exhibited outstanding flexibility and miniaturization properties compared to those of the previously discussed antennas.

II. ANTENNA CONFIGURATION

When designing implantable antennas, the choice of fabrication material plays a crucial role. Flexible materials are preferred for easy implantation in electronic devices (BMI) and the human torso [15]. They can withstand tissue/muscle movement without causing damage and do not impact antenna performance when subjected to physical or dimensional changes [16].

Figure 2 displays the conceived antenna, with minuscule dimensions of 7 mm × 7 mm and a flexible biocompatible polyamide material (permittivity, ε_r = 4.2 and tangent loss, tanδ = 0.002) was used as the substrate layer. To ensure safety and prevent direct contact with brain tissues, a polyamide superstrate layer was added as insulation on the antenna's radiating patch. The circular cut at the center of the radiating patch contributes to the antenna's dual-band functionality. Additionally, a pendulum-shaped circular slot connected to the outer body enables tuning and significant miniaturization of the implantable antenna.

Tuning and matching the frequency are crucial for achieving the desired bandwidth within the considered ISM bands. To achieve this, L-shaped and rectangular cuts were introduced in the ground plane. A shorting pin with a radius of 0.3 mm was used between the ground and patch to achieve the desired frequency band and antenna miniaturization. The antenna was excited using a 50Ω coaxial feed with a radius of 0.3 mm placed at the circular slot. The desired bandwidth characteristics at the target frequency bands were achieved

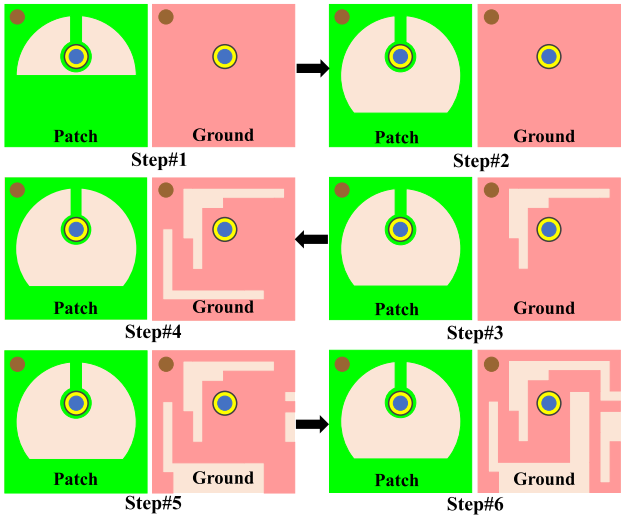

FIGURE 3. Optimization steps to achieve the desired antenna geometry and performance for BMI devices.

by positioning the feed at the location of maximum current distribution.

A. WORKING PRINCIPAL OF THE CONCEIVED DUAL-BAND ANTENNA

The development of BMI devices is challenging owing to their high power consumption; therefore, a dual-band design is considered for switching between wake-up and sleep modes to conserve battery power [19], [20]. Consequently, implantable devices have a longer lifespan, and interference issues are reduced. When the antenna is in sleep mode in the 2.45 GHz ISM band, no data is transmitted. The power consumption of implantable devices is much lower in the 2.45 GHz band. When the antenna is in the wake-up mode, it transmits data at a frequency of 915 MHz.

B. DESIGNING STEPS

The conceived dual-band antenna was designed and simulated in six successive steps to achieve the required bandwidth for better operation in the ISM (915 MHz and 2.45 GHz) bands. Fig. 3 illustrates a step-by-step modification in radiating patch and ground plane. The antenna underwent design and fabrication modifications by altering the shape of the radiating patch to a rectangular pendulum shape and incorporating an open-end slotted ground plane. The impact of these modifications on the reflection coefficient (S_{11}) was observed, as depicted in Fig. 4.

Initially, a simple ground plane was employed, as shown in the first step. However, this configuration resulted in an undesired resonance at a higher frequency of 3.65 GHz, with S_{11} falling below -10 dB. To address this issue, a circular slot was introduced in the patch during the second step. This adjustment led to the appearance of three resonances at frequencies of 1.25 GHz, 2.7 GHz, and 4.2 GHz. The resonances at the higher frequencies (2.7 GHz and 4.2 GHz)

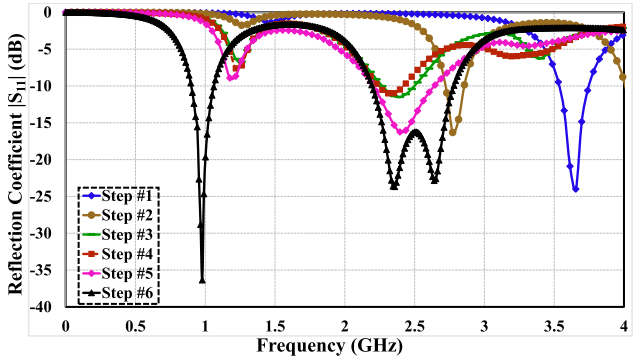

FIGURE 4. Effects of basic steps on reflection coefficient (S_{11}).

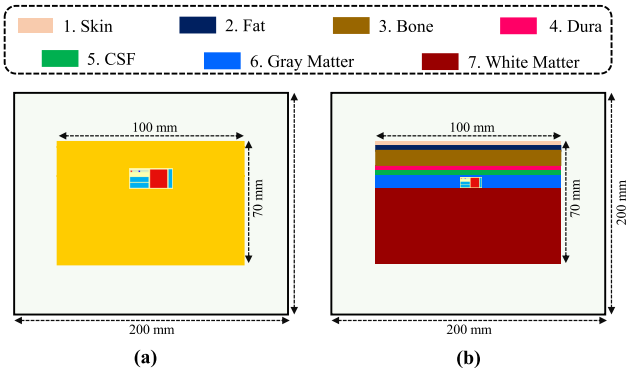

FIGURE 5. Detailed architecture and dimension of implantable antenna-embedded BMI device.

exhibited S_{11} values below -10 dB, while the resonance at the lower frequency (1.25 GHz) had an S_{11} value above -10 dB.

To further fine-tune the frequencies and improve the matching, additional L-shaped and rectangular slots were created in the ground plane. The third and fourth steps involved the addition of an L-shaped and an inverted L-shaped slot, respectively, which helped shift the frequency towards the lower bands. In the fifth step, rectangular slots were placed on the edges of the ground plane to adjust the higher ISM frequency band (2.45 GHz) to its center frequency.

However, for tuning the lower frequency band, more slots were added in the final sixth step. Figure 4 demonstrates that these slots successfully tuned the lower ISM band (0.915 GHz) to its center frequency. Consequently, in the final step, the antenna design achieved dual resonances at 915 MHz and 2450 MHz, with S_{11} values below -25 dB. These lower S_{11} values indicate the reliable communication capability of the conceived antenna design.

C. OPTIMIZATION OF THE ANTENNA WITHIN THE DEVICE AND IN SEVEN-LAYER BRAIN MODEL

The conceived antenna was designed and analyzed using the finite element method in an ANSYS high-frequency structure simulator (HFSS). To reduce the simulation time, the antenna was designed at the 15 mm depth in a homogeneous skin phantom (HSP) with dimensions of 100 mm × 100 mm × 70 mm and HSP is kept at the center of the radiation box with dimensions of 200 mm × 200 mm × 200 mm, as shown in Fig. 5(a). Furthermore, a heterogeneous seven-layer brain model was designed to validate the performance of the antenna, as shown in Fig. 5(b). Due to frequency dependence, the different layers of the human head model contain different values of permittivity (ε_r) and electrical conductivity (σ) [17], [18]. The permittivity (ε_r) and conductivity (σ) values at different ISM (0.915 GHz and 2.45 GHz) bands of different layers of the human brain model are listed in Table 2.

Furthermore, a BMI device model composed of a casing, antenna, electronic package, sensors, batteries, and power manager is constructed in HFSS to investigate the effect of electronic components on the performance of the antenna, as shown in Fig. 6. By including the conceived implanted

TABLE 2. Electrical parameters of different phantoms of the seven-layer brain model.

Phantom	Thickness	915 MHz		2.45 GHz	
	(mm)	Permittivity	Conductivity (S/m)	Permittivity	Conductivity (S/m)
Skin	1.5	41.3	0.872	38	1.46
Fat	2	5.46	0.00514	5.28	0.105
Bone	7	12.4	0.145	11.4	0.394
Dura	2	44.4	0.966	42	1.67
Cerebral Fluid	3	68.6	2.42	66.2	3.46
Bray Matter	6	52.7	0.949	48.9	1.81
White Matter	55	38.8	0.595	36.2	1.21

antenna in the HSP and seven-layer brain model, the S_{11} analysis was completed and the effects of the device package were also considered. The comparison of simulated S_{11} in different scenarios such in HSP, modeled BMI, and seven layed brain model in HFSS is given in Fig. 7. As shown in Fig. 7, the simulated S_{11} plot of the antenna in BMI device model closely matched to the necessary ISM (0.915 GHz and 2.45 GHz) frequency bands as in the HSP. However, the S_{11} plot moved to the upper-frequency spectrum when the device was introduced in the HSP. Subsequently, the frequency band shifts to a lower frequency in the seven-layer brain model.

III. PARAMETRIC ANALYSIS

Parametric analysis is crucial for optimizing antennas in different scenarios. In this section, different antenna parameters and their effects on the performance of the antenna are discussed. Parametric analysis was performed by placing the conceived antenna at the 15 mm depth of the HSP with the same properties and dimensions as those described in Fig. 5(a), and the reflection coefficient was observed by varying the parameters of the antenna. A detailed study of all parameters of the conceived antenna is beyond the scope of this study.

A. OPTIMIZATION OF THE ANTENNA USING STRIP (S_1)

The ground plane strip (S_1) significantly affects the impedance Conformity of the antenna. Fig 8. shows how S_1 affects the return loss of the antenna, with the strip alteration clearly showing slight fluctuations in the lower resonance;

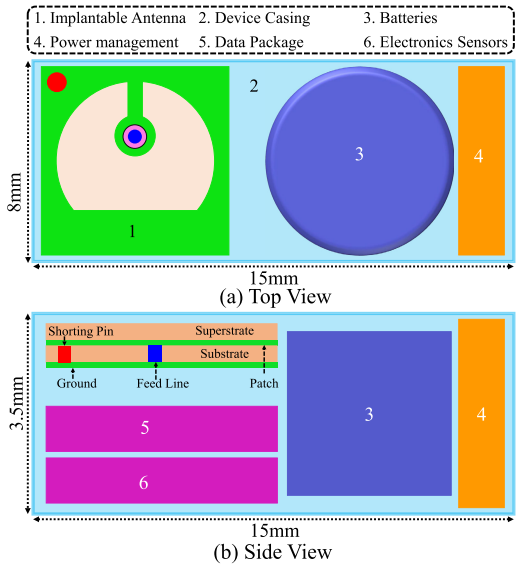

FIGURE 6. Simulation environments of the conceived dual-band antenna. (a) Homogeneous skin phantom (HSP). (b) Seven-layer brain model.

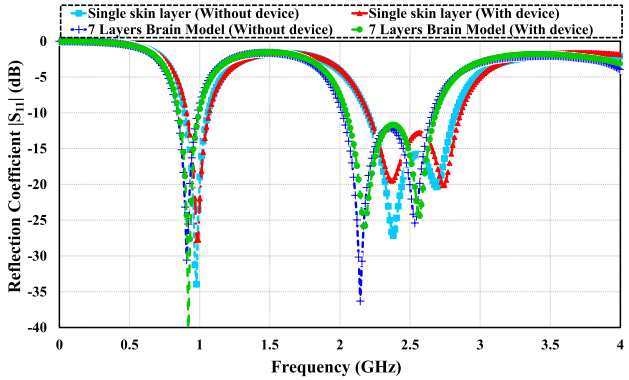

FIGURE 7. Reflection coefficient (S_{11}) analysis of the conceived antenna in different environments (HSP, BMI device, and seven-layer brain model).

moreover, decreasing the strip size lowers the dip on the 2.45 GHz. The resonance eventually divides into two frequency bands at S_1 = 1.0 mm, while on the opposite side, the increase in strip length causes the resonance in the S_{11} plot to shift to a higher resonance. Because the bandwidth of the higher band finally decreases. Therefore, a 2.0 mm length is chosen for strip S_1.

B. OPTIMIZATION OF THE ANTENNA USING PARAMETER (S_2)

The parameter (S_2) of the radiating patch is also crucial for the stability of the conceived antenna. Fig. 9 highlights the impact of parameter S_2, which shows that the variation in the parameter length has an insignificant effect on the lower resonance. It was observed from the length variation that the increment in the length of the parameter S_2 lowers the dip at 2.45 GHz and even vanishes the frequency band at 2.45 GHz at (S_2) = 3.05 mm, whereas the decrease in the

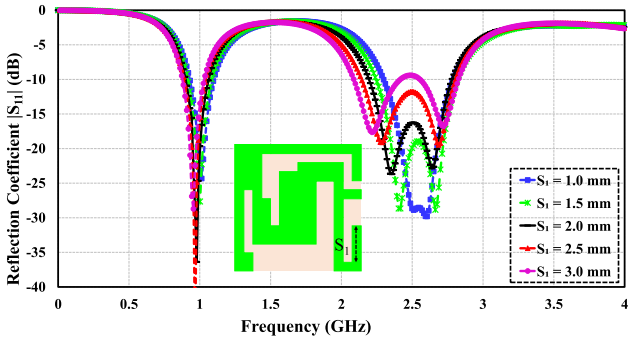

FIGURE 8. S_{11} analysis by changing the length of strip S_1 in ground.

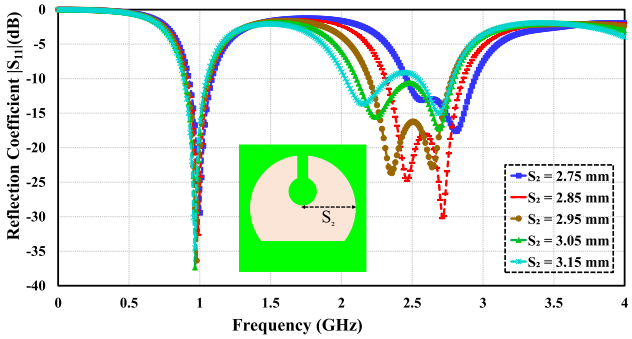

FIGURE 9. S_{11} analysis by changing the length of circular cut S_2 in ground.

parameter causes a rapid shift of the frequency band to a higher resonance. Therefore, the parameter length (S_2) is set to 2.95 mm to achieve dual-band resonance.

C. OPTIMIZATION OF THE ANTENNA USING SHORTING PIN

The conceived antenna is miniaturized by employing a shorting pin between the ground plane and radiating patch. However, to achieve antenna minusculeness, the location of the shorting pin and its optimal position is crucial. Fig. 10 shows the effect on the reflection coefficient (S_{11}) by changing the position of the shorting pin of the antenna, and the analysis was performed using four comparative designs. Design 1 resonates at 1.6 GHz with S_{11} < -15 dB, whereas design 2 gives two resonances at 850 MHz and 2.45 GHz, but these frequency bands are not reliable for communication. A small deviation occurred at the frequency bands by moving the shorting pin to position V_3. However, the final designs provide dual bands at 915 and 2450 MHz with S_{11} > -20 dB.

IV. RESULTS

As discussed earlier, the conceived dual-band antenna was designed and simulated at the 15 mm of an HSP box using the finite element method. The dielectric properties of the HSP are frequency-dependent, which provides stable and reliable results for the antenna. For the optimized antenna, a seven-layer brain model was designed. To investigate a

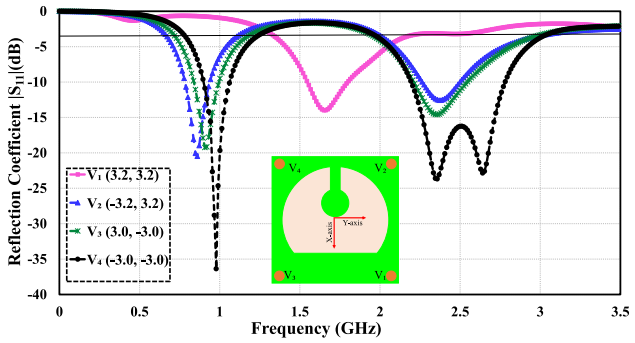

FIGURE 10. S_{11} Analysis by varying the shorting pin position of the multiband antenna (unit: mm).

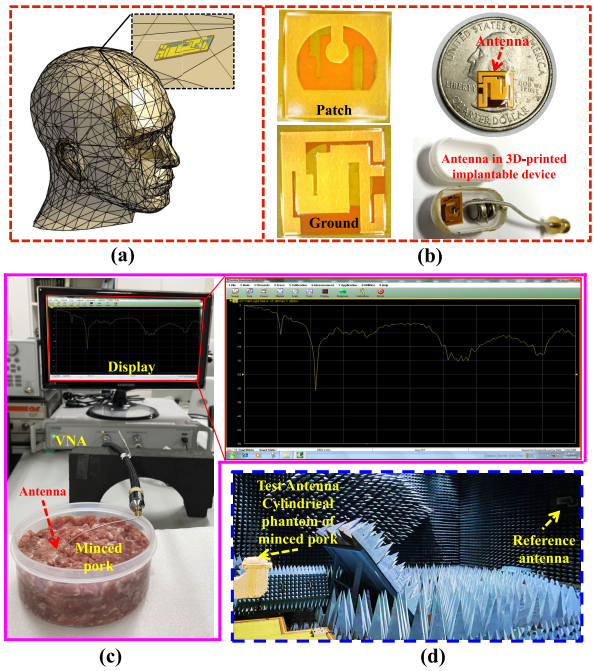

FIGURE 11. Fabricated prototypes and simulation and measurement setups. (a) conceived antenna in the heterogeneous realistic head model. (b) Fabricated antenna prototype in the 3D-printed implantable device. (c) S_{11} Measuring setup in minced pork meat. (d) Radiation pattern testing of the antenna in Cylindrical phantom of minced pork.

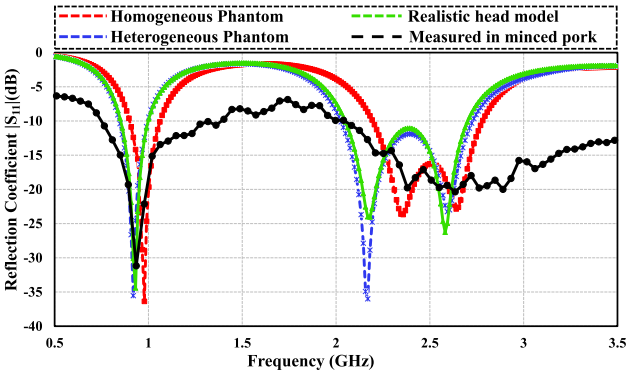

FIGURE 12. Analysis of simulated and measured S_{11} of the conceived implantable antenna.

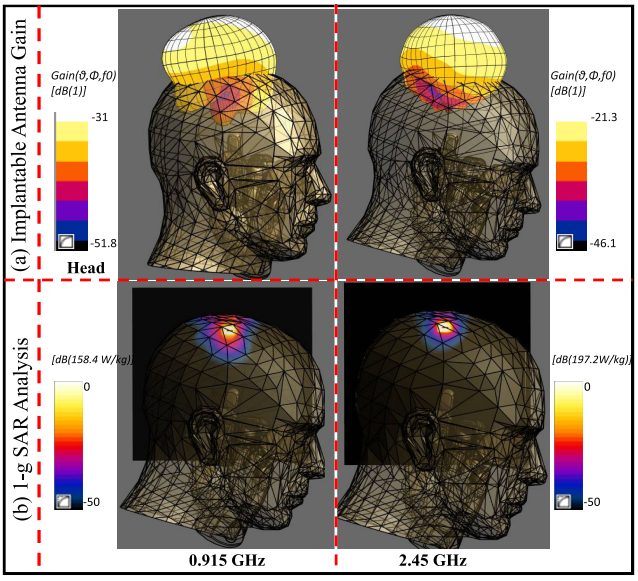

FIGURE 13. 3D gain patterns and SAR distributions of the antenna simulated in the realistic human head. (a) 3D radiation patterns at 915 MHz and 2.45 GHz, respectively. (b) SAR distributions on the human head at 915 MHz and 2.45 GHz, respectively.

more accurate and practical scenario, the implantable antenna system was first analyzed at 15 mm depth using a heterogeneous realistic head model, as shown in Fig. 11 (a), and a prototype model of the conceived implantable antenna was fabricated and placed in a 3D dummy capsule for testing purpose, as shown in Fig. 11 (b). Figs. 11 (c) and (d) show the S_{11} measurement setup and radiation chamber, respectively. The conceived antenna embedded in a dummy capsule is placed in a canonical container filled with minced pork meat for S_{11} and radiation measurement.To excite the patch of the conceived antenna SMA connector is used.

Fig. 12 shows a comparison of the reflection coefficient (S_{11}) of the conceived antenna in different simulation environments and the measured values. The conceived antenna embedded in modeled BMI device is simulated in different environments such as HSP, BMI device, and seven-layer brain model and S_{11} is measured by placing the conceived antenna in a 3D dummy capsule device. A small shift in the reflection coefficient was observed owing to the variations in the electrical properties of the skin tissue [21]. Furthermore, the performance of the antenna is also validated by considering the effect of the microelectronic components of the BMI device.

The results show that the reflection coefficient value at a higher ISM (2.45 GHz) band is decreased by introducing an implantable device in a heterogeneous phantom and realistic head model. Remarkably, the heterogeneous environment and electronic components had an insignificant effect on the lower ISM (0.915 GHz) band, while a slight shift in the resonance spectrum was observed at higher frequencies in the proximity of batteries and electronic components. In HSP,

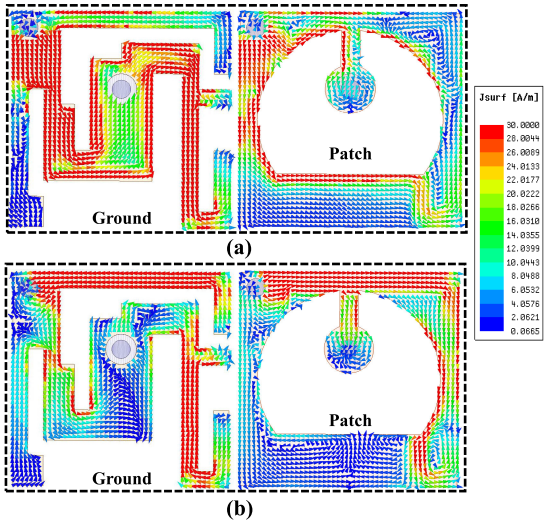

FIGURE 14. Current distribution on the surface of the conceived antenna. (a) 915 MHz. (b) 2.45 GHz.

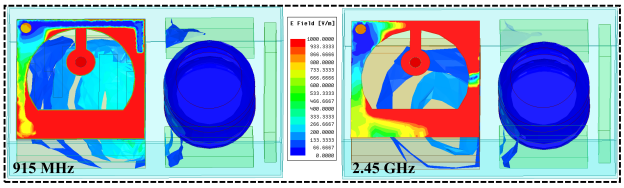

FIGURE 15. E-field distribution on the circuitry inside the BMI device at two frequencies (915 MHz and 2.45 GHz) (scale: V/m).

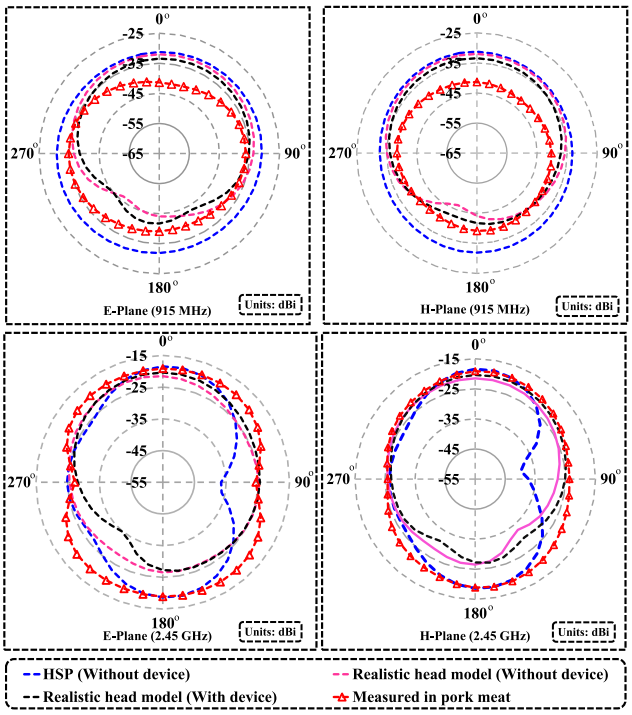

FIGURE 16. Simulated and measured radiation pattern of the conceived implantable antenna.

the conceived antenna has simulated bandwidths of 163 and 585 MHz, and peak gains of -28.3 and -18.5 dBi at 915 MHz and 2.45 GHz, respectively. In a heterogeneous body environment, the simulated bandwidths of the conceived antenna are 155 MHz (840-995 MHz) and 723 MHz (2.025-2.728 GHz). Despite the small deviation owing to the air space between the superstrate layer and the antenna radiator, the measured reflection coefficients were nearly identical. It is worth noting that the measured return loss values exhibit wideband characteristics on both frequency bands.

Furthermore, for S_{11}, gain, and SAR analysis in a heterogeneous environment commercial Sim4Life software is used. Moreover, the implantable antenna gain was calculated in the heterogeneous-head model at both resonance frequencies, as shown in Fig. 13. The antenna worked perfectly in a heterogeneous environment and radiated the main lob outside the head model, which is vital for BMI communication because most of the power can be received by the outside device. The simulated peak gain in the heterogeneous head model was -31 and -21.3 dBi at lower (0.915 GHz) and higher (2.45 GHz) frequency bands, respectively; which closely matches with the simulated gain values in the HSP environment.

A. CURRENT DISTRIBUTION AND RADIATION PATTERNS

The current distribution over the radiator is an important parameter of the antenna to achieve the required resonance of the under-consideration frequencies [22], [23]. Fig. 14 shows the current vector distribution at the two resonance frequencies (915 MHz and 2450 MHz). It is evident that the current shifts from the ground plane feed line toward the radiating patch through the feed line, and the current density is at its highest near the shorting pin at both resonance frequencies (0.915 GHz and 2.45 GHz). The current moves in the same direction and does not change its direction which corresponds to $\lambda/4$ monopole resonance mode at the lower ISM (915 MHz) band, as shown in Fig. 14(a). Similarly, at 2.45 GHz resonance frequency maximum current is observed over the upper slot/arm of both ground and radiating patch. From Fig. 14(b), it can be seen that the current changes its path and moves in the opposite directions which corresponds to $\lambda/2$ monopole resonance mode.

Furthermore, for practical consideration, the batteries and other electrical components are placed inside BMI container along with the implantable antenna. However, the BMI component is placed in such a way that they do not affect the performance of the antenna. The electric field distribution is shown in Fig. 15. From Fig. 15, it can be seen that there is negligible effect on the electrical components and the maximum electric field can be seen on the surface of the antenna at both frequencies (915 MHz and 2.45GHz).

Fig. 16 shows a comparison of the simulated and measured far-field radiation patterns of the antenna. The radiation pattern of the conceived antenna is simulated in different environments such as in HSP without modeled device and in a realistic head model with and without modeled BMI

TABLE 3. Link budget parameters for the conceived antenna.

Parameters	Variable	Value
Resonance frequency	f_r (MHz)	915/2450
Noise power density	N_o (dB/Hz)	-203.93
Transmitter power	P_t (dBW)	-46.02
Temperature	T_o (Kelvin)	273
Free space path loss	L_f (dB)	Distance dependent
Transmitter antenna gain	G_t (dBi)	-28.3/-18.5
Receiver antenna gain	G_r (dBi)	2.15
Available power	A_p (dB)	Distance dependent
Required power	R_p (dB)	Adaptive (Bit rate)
Margin	A_p - R_p (dB)	Fig. 15

device in HFSS. For measured radiation pattern the conceived antenna is placed inside the canonical box filled with minced pork. Irrespective of the environment, the radiation patterns at the higher ISM (2.45 GHz) band are indistinguishable. In contrast, at a lower ISM (0.915 GHz) band, the measured radiation pattern shows some contradiction with the simulated patterns. The radiation pattern is measured in a canonical box filled with minced pork which is larger in size with respect to the HSP box in HFSS. Therefore, the antenna shows a smaller peak gain value at the lower band. However, the peak gain values obtained in various environments satisfy the criteria for the ISM-band telemetry radiation pattern of the traditional implanted antenna.

B. SAR ANALYSIS

SAR analysis is mandatory to meet the safety standards of IEEE for biomedical devices. To ensure the safety of patients, 1.6 and 2 W/kg are the limits approved by the IEEE for 1-g and 10-g tissues, respectively [8], [25]. Therefore, the SAR was calculated in a realistic human head model for both resonance frequencies, as shown in Fig. 13, and a transmitter power of 1 W was used to obtain the SAR values. It is recommended that the maximum 1 g input power never exceeds 10 mW (10 dBm) at 915 MHz and 8.1 mW (9.1 dBm) at 2.45 GHz to maintain the SAR within the imposed limits. Although the calculated input power values do not match the prescribed values, the input power to implantable antennas is limited to 25 μW [5]. Based on these calculations, the SAR values of the implantable antenna meet IEEE regulations and can be used in BMI devices.

V. LINK BUDGET ANALYSIS

For a detailed study of the data telemetry range of the device, we computed the link budget from an in-body transmitter to an external device scenario. This calculation is the sum of different types of power losses, such as free-space losses (L_f), cable losses, material loss, and impedance mismatch [19].

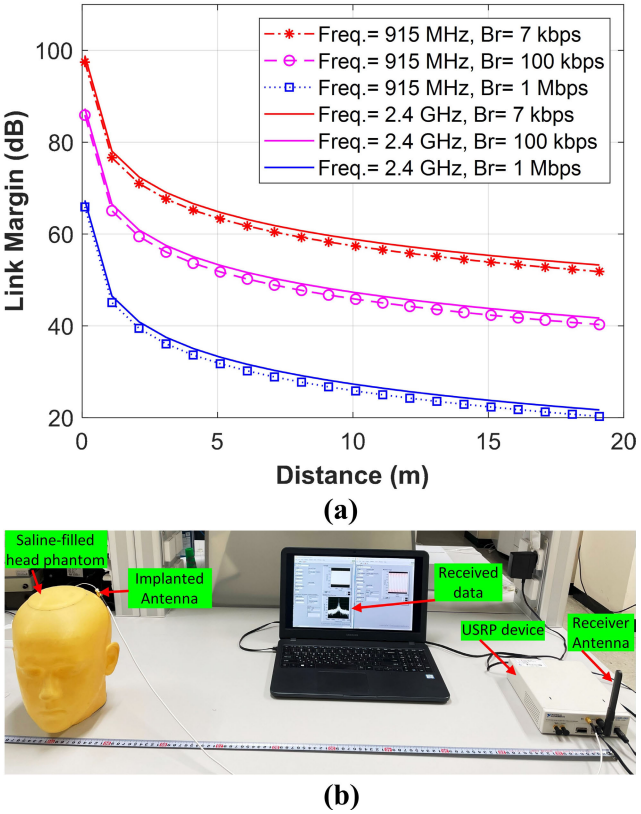

FIGURE 17. Transmission range of the antenna at 915 and 2400 MHz at different data rates. (a) Link margin analysis. (b) real-time data communication and link analysis of dual-band implantable antenna with NI-USRP.

Moreover, this analysis explains the data range at different lengths between the implanted devices and external sources. Such scenarios are noteworthy in hospitals during treatment, primarily when wireless communicating implantable devices are studied. The acceptable power margin for persistent and reliable communication should be greater than 20 dB, which is calculated by taking the difference between the available antenna power (A_p) and the required power (R_p) to operate the device. The parameters required to calculate the link budget are listed in Table 3. The required power (R_p) can be calculated as

$$R_p(dB) = (E_b/N_0) + KT_0 + B_r$$

where E_b/N_0 represents the ideal phase-shift keying constant (9.6 dB), $K = 1.38 \times 10^{-23}$ is Boltzmann's constant, T_0 is the temperature in Kelvin, and B_r represents the transmission rate in Mb/s or kb/s. To avoid interference with surrounding services, the effective isotropic radiated power (EIRP) is also restricted to the maximum input power for implantable antennas [8]. In the lower-frequency spectrum, the signal propagates more reliably in the body than at high frequencies. The EIRP must be less than or equal to $EIRP_{max}$ = 36 dBm for the 915 and 2450 MHz bands.

The active electronics circuits need a power source to operate and their power is limited [4]. In the BMI device,

silver oxide batteries with 20 mW power were used to supply 3V at 55 mAh to the circuit for 8–9 hours continuously. By considering this information, the transmitter power (P_t) is kept at -16 dBm for brain implantations, which is lower than the maximum allowed input power. Hence, B_r was set at 100 kb/s, as brain implants require a high data rate. The total available power of an antenna can be calculated as:

$$A_p(dB) = P_{Tx} + G_{Tx} + G_{Rx} - L_f$$

where P_{Tx} denotes the power (dB) transmitted, and G_{Tx} and G_{Rx} are the gain values of the transmitter and receiver, respectively. L_f (dB) is the free-space loss value that depends on the distance (d) between the transmitter and receiver, which can be calculated as

$$L_f(dB) = 20 \times [log(4\pi d/\lambda)]$$

It is evident from the margin vs. distance plot, as shown in Fig. 17(a), that 1 Mb/s data can be easily transmitted up to a distance of 10 m. The link margin and data analysis in real-time was carried out in a realistic human head phantom filled with saline solution and NI-USRP, as shown in Fig. 17 (b).

VI. CONCLUSION

In this study, a minuscule dual-band implantable antenna was developed for a BMI device. The conceived antenna has a small dimension of 7 mm × 7 mm × 0.2 mm (9.8 mm^3) that can be accommodated in the small BMI device. The dual-band resonance characteristic of the antenna was utilized as a switch between the sleep/wakeup mode to reduce power consumption. The radiation patterns and reflection coefficients of the fabricated antenna prototype were measured to validate the performance of the antenna for BMI communication. The power link budget suggested that the antenna system can transmit a signal of up to 10 m at a data rate of 100 kbps. The higher gain and lower SAR values indicated that the conceived design is a vital choice for future high-data-rate BMI devices.

ACKNOWLEDGMENT

(Naeem Abbas, Sana Ullah, and Zubair Bashir are co-first authors.)

REFERENCES

[1] A. Basir, Y. Cho, I. Ali Shah, S. Hayat, S. Ullah, M. Zada, S. A. A. Shah, and H. Yoo, "Implantable and ingestible antenna systems: From imagination to realization," 2023, *arXiv:2306.02434*.
[2] M. A. Lebedev and M. A. L. Nicolelis, "Brain-machine interfaces: Past, present and future," *Trends Neurosci.*, vol. 29, no. 9, pp. 536–546, Sep. 2006.
[3] L. Song and Y. Rahmat-Samii, "An end-to-end implanted brain-machine interface antenna system performance characterizations and development," *IEEE Trans. Antennas Propag.*, vol. 65, no. 7, pp. 3399–3408, Jul. 2017, doi: 10.1109/TAP.2017.2700163.
[4] B. Rana, J.-Y. Shim, and J.-Y. Chung, "An implantable antenna with broadside radiation for a brain-machine interface," *IEEE Sensors J.*, vol. 19, no. 20, pp. 9200–9205, Oct. 2019.
[5] A. Kiourti and K. S. Nikita, "A review of in-body biotelemetry devices: Implantables, ingestibles, and injectables," *IEEE Trans. Biomed. Eng.*, vol. 64, no. 7, pp. 1422–1430, Jul. 2017, doi: 10.1109/TBME.2017.2668612.
[6] M. Zada and H. Yoo, "A miniaturized triple-band implantable antenna system for bio-telemetry applications," *IEEE Trans. Antennas Propag.*, vol. 66, no. 12, pp. 7378–7382, Dec. 2018.
[7] A. Kiourti and K. S. Nikita, "Miniature scalp-implantable antennas for telemetry in the MICS and ISM bands: Design, safety considerations and link budget analysis," *IEEE Trans. Antennas Propag.*, vol. 60, no. 8, pp. 3568–3575, Aug. 2012, doi: 10.1109/TAP.2012.2201078.
[8] T.-F. Chien, C.-M. Cheng, H.-C. Yang, J.-W. Jiang, and C.-H. Luo, "Development of nonsuperstrate implantable low-profile CPW-fed ceramic antennas," *IEEE Antennas Wireless Propag. Lett.*, vol. 9, pp. 599–602, 2010, doi: 10.1109/LAWP.2010.2053342.
[9] E. A. Mainul and M. F. Hossain, "Design of a compact implantable antenna in seven-layer brain phantom for brain-machine interface applications," in *Proc. Int. Conf. Electron., Commun. Inf. Technol. (ICECIT)*, Sep. 2021, pp. 1–4, doi: 10.1109/ICECIT54077.2021.9641415.
[10] S. Hout and J.-Y. Chung, "Design and characterization of a miniaturized implantable antenna in a seven-layer brain phantom," *IEEE Access*, vol. 7, pp. 162062–162069, 2019, doi: 10.1109/ACCESS.2019.2951489.
[11] A. Abdi, F. Ghorbani, H. Aliakbarian, T. K. Geok, S. K. A. Rahim, and P. J. Soh, "Electrically small spiral PIFA for deep implantable devices," *IEEE Access*, vol. 8, pp. 158459–158474, 2020, doi: 10.1109/ACCESS.2020.3018882.
[12] I. A. Shah, M. Zada, and H. Yoo, "Design and analysis of a compact-sized multiband spiral-shaped implantable antenna for scalp implantable and leadless pacemaker systems," *IEEE Trans. Antennas Propag.*, vol. 67, no. 6, pp. 4230–4234, Jun. 2019, doi: 10.1109/TAP.2019.2908252.
[13] A. Iqbal, M. Al-Hasan, I. B. Mabrouk, and M. Nedil, "Scalp-implantable MIMO antenna for high-data-rate head implants," *IEEE Antennas Wireless Propag. Lett.*, vol. 20, no. 12, pp. 2529–2533, Dec. 2021, doi: 10.1109/LAWP.2021.3117345.
[14] N. Abbas, S. A. A. Shah, A. Basir, Z. Bashir, A. Akram, and H. Yoo, "Miniaturized antenna for high data rate implantable brain-machine interfaces," *IEEE Access*, vol. 10, pp. 66018–66027, 2022, doi: 10.1109/ACCESS.2022.3184778.
[15] S. Das and D. Mitra, "A compact wideband flexible implantable slot antenna design with enhanced gain," *IEEE Trans. Antennas Propag.*, vol. 66, no. 8, pp. 4309–4314, Aug. 2018.
[16] A. C. Durgun, C. A. Balanis, C. R. Birtcher, and D. R. Allee, "Design, simulation, fabrication and testing of flexible bow-tie antennas," *IEEE Trans. Antennas Propag.*, vol. 59, no. 12, pp. 4425–4435, Dec. 2011.
[17] S. Gabriel, R. W. Lau, and C. Gabriel, "The dielectric properties of biological tissues: II. Measurements in the frequency range 10 Hz to 20 GHz," *Phys. Med. Biol.*, vol. 41, no. 11, pp. 2251–2269, Nov. 1996.
[18] N. Abbas, A. Basir, A. Iqbal, M. Yousaf, A. Akram, and H. Yoo, "Ultra-miniaturized antenna for deeply implanted biomedical devices," *IEEE Access*, vol. 10, pp. 54563–54571, 2022.
[19] N. Ganeshwaran, J. K. Jeyaprakash, M. G. N. Alsath, and V. Sathyanarayanan, "Design of a dual-band circular implantable antenna for biomedical applications," *IEEE Antennas Wireless Propag. Lett.*, vol. 19, no. 1, pp. 119–123, Jan. 2020, doi: 10.1109/LAWP.2019.2955140.
[20] C. Liu, Y.-X. Guo, and S. Xiao, "Minuscule dual-band antenna for implantable devices," *IEEE Antennas Wireless Propag. Lett.*, vol. 11, pp. 1508–1511, 2012, doi: 10.1109/LAWP.2012.2233705.
[21] S. A. A. Shah and H. Yoo, "Scalp-implantable antenna systems for intracranial pressure monitoring," *IEEE Trans. Antennas Propag.*, vol. 66, no. 4, pp. 2170–2173, Apr. 2018.
[22] J.-Z. Bao, S.-T. Lu, and W. D. Hurt, "Complex dielectric measurements and analysis of brain tissues in the radio and microwave frequencies," *IEEE Trans. Microw. Theory Techn.*, vol. 45, no. 10, pp. 1730–1741, Oct. 1997, doi: 10.1109/22.641720.
[23] Z. Bao, Y.-X. Guo, and R. Mittra, "Single-layer dual-/tri-band inverted-F antennas for conformal capsule type of applications," *IEEE Trans. Antennas Propag.*, vol. 65, no. 12, pp. 7257–7265, Dec. 2017.
[24] S. A. A. Shah, M. F. Khan, S. Ullah, A. Basir, U. Ali, and U. Naeem, "Design and measurement of planar monopole antennas for multi-band wireless applications," *IETE J. Res.*, vol. 63, no. 2, pp. 194–204, Mar. 2017.
[25] G. Ciuti, A. Menciassi, and P. Dario, "Capsule endoscopy: From current achievements to open challenges," *IEEE Rev. Biomed. Eng.*, vol. 4, pp. 59–72, 2011.

NAEEM ABBAS received the B.Sc. degree in telecommunication engineering from the University College of Engineering and Technology (UCET), Islamia University Bahawalpur, Pakistan, in 2018, and the M.Sc. degree in telecommunication engineering from the University of Engineering and Technology (UET), Taxila, Pakistan, in 2021. He is currently pursuing the Ph.D. degree in electronic engineering with Hanyang University, Seoul, South Korea. His current research interests include implantable antennas and systems, passive chipless RFID tags, wireless power transfer, wireless communication, the Internet of Things (IoT), and image processing.

SANA ULLAH (Graduate Student Member, IEEE) received the B.Sc. and M.Sc. degrees in telecommunication engineering from the University of Engineering and Technology, Peshawar, Pakistan, in 2013 and 2016, respectively, and the Ph.D. degree in electronic engineering from Hanyang University, Seoul, South Korea, in 2022.

He has been the Samsung Foundation Global Hope Scholar, since 2018. Currently, he is a Postdoctoral Researcher with Hanyang University. His current research interests include 60 GHz MIMO antennas, implantable antennas, metamaterial, RF coils for MRI, micro-coil for blood vessel imaging, wireless MRI, flexible and stretchable RF coils, and sensors with MRI receive coil. In 2018, he received the Best Student Paper from the Korean Institute of Electromagnetic Engineering and Science (KIEES).

ZUBAIR BASHIR received the B.Sc. degree in telecommunication engineering from the University of Engineering and Technology, Taxila, Pakistan, in 2019, where he is currently pursuing the M.Sc. degree with the Telecommunication Engineering Department. He joined the ACT-SENA Research Group, University of Engineering and Technology, Taxila. His current research interests include implantable antennas, meta-material, multiple-input and multiple-output (MIMO) systems, and reconfigurable antennas.

ABDUL BASIR (Member, IEEE) was born in Khyber Pukhtoonkhwa, Pakistan, in 1989. He received the B.Sc. degree in telecommunication engineering from the University of Engineering and Technology, Peshawar, Pakistan, in 2015, and the M.S./Ph.D. degree in electronic engineering from Hanyang University, Seoul, South Korea, in 2021. Currently, he is a Postdoctoral Researcher with Hanyang University. His current research interests include implantable antennas and systems, biomedical circuits, wearable antennas, MIMO communication, metamaterial, dielectric resonator antennas, reconfigurable antennas, long-range wireless power transfer, and the wireless charging of biomedical implants. He was awarded Silver Prize for the best student paper awards in the 2018 and 2019 Student Paper Contests, IEEE Seoul Section. His collaborated paper was awarded the 2019 Best Paper Award by the IEEE AP/MTT/EMC Joint Chapter Malaysia. He received the Third Prize for the 2018 Best Student Paper Completion by the Korea Communications Agency (KCA) and the Korean Institute of Electromagnetic Engineering and Science (KIEES).

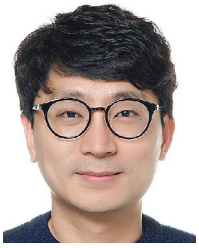

HYOUNGSUK YOO (Senior Member, IEEE) received the B.Sc. degree in electrical engineering from Kyungpook National University, Daegu, South Korea, in 2003, and the M.Sc. and Ph.D. degrees in electrical engineering from the University of Minnesota, Minneapolis, MN, USA, in 2006 and 2009, respectively.

In 2009, he joined the Center for Magnetic Resonance Research, University of Minnesota, as a Postdoctoral Associate. In 2010, he joined Cardiac Rhythm Disease Management, Medtronic, MN, USA, as a Senior Electromagnetic (EM)/MRI Scientist. From 2011 to 2018, he was an Associate Professor with the Department of Biomedical Engineering, School of Electrical Engineering, University of Ulsan, Ulsan, South Korea. Since 2018, he has been a Professor with the Department of Biomedical Engineering and the Department of Electronic Engineering, Hanyang University, Seoul, South Korea. He has been the Chief Executive Officer (CEO) of Electro Magnetics and Magnetic Resonance (E2MR), a startup company, Seoul, South Korea, since 2017. His current research interests include EM theory, numerical methods in EMs, metamaterials, antennas, implantable devices, and magnetic resonance imaging in high-magnetic field systems. He received the Third Prize for the Best Student Paper at the 2010 IEEE Microwave Theory and Techniques Society International Microwave Symposium.